

ORIGINAL ARTICLE

Parvalbumin-Positive Interneurons Regulate Neuronal Ensembles in Visual Cortex

Masakazu Agetsuma^{1,2,3,5}, Jordan P. Hamm¹, Kentaro Tao⁴, Shigeyoshi Fujisawa⁴ and Rafael Yuste¹

¹Neurotechnology Center, Department of Biological Sciences, Columbia University, 550 West 120 Street, Box 4822, New York, NY 10027, USA, ²Japan Science and Technology Agency, PRESTO, 4-1-8 Honcho, Kawaguchi, Saitama 332-0012, Japan, ³The Institute of Scientific and Industrial Research, Osaka University, Mihogaoka 8-1, Ibaraki, Osaka 567-0047, Japan, ⁴RIKEN Brain Science Institute, 2-1 HiroSawa, Wako, Saitama 351-0106, Japan and ⁵Present address: National Institute for Physiological Sciences, Division of Homeostatic Development, 38 Nishigohnaka Myodaiji-cho, Okazaki, Aichi 444-8585, Japan

Address correspondence to Masakazu Agetsuma, Department of Biomolecular Science and Engineering, The Institute of Scientific and Industrial Research, Osaka University, Mihogaoka 8-1, Ibaraki, Osaka 567-0047, Japan. Email: ms9@sanken.osaka-u.ac.jp, age@nips.ac.jp

Abstract

For efficient cortical processing, neural circuit dynamics must be spatially and temporally regulated with great precision. Although parvalbumin-positive (PV) interneurons can control network synchrony, it remains unclear how they contribute to spatio-temporal patterning of activity. We investigated this by optogenetic inactivation of PV cells with simultaneous two-photon Ca^{2+} imaging from populations of neurons in mouse visual cortex *in vivo*. For both spontaneous and visually evoked activity, PV interneuron inactivation decreased network synchrony. But, interestingly, the response reliability and spatial extent of coactive neuronal ensembles during visual stimulation were also disrupted by PV-cell suppression, which reduced the functional repertoire of ensembles. Thus, PV interneurons can control the spatio-temporal dynamics of multineuronal activity by functionally sculpting neuronal ensembles and making them more different from each other. In doing so, inhibitory circuits could help to orthogonalize multicellular patterns of activity, enabling neural circuits to more efficiently occupy a higher dimensional space of potential dynamics.

Key words: interneuron, multineuronal response reliability, network synchrony, optogenetics, two-photon imaging

Introduction

In cortical circuits, neurons work together as a group to process information. The input of a single neuron alone is typically not enough to make a target cell fire; coincident inputs from multiple excitatory neurons within a certain time window are required to depolarize the membrane potential beyond a threshold and trigger firing in the target cell, thereby resulting in a relay of information. Thus, the cooperative or synchronous activity of neural populations is likely critical for circuit computations (Abeles 1991). But synchronous activity must be precisely regulated. It is known that neural responses to sensory

stimuli are heterogeneous among neurons belonging to the same group, and even within the same neuron, across brief timescales. Moreover, recent theoretical studies have suggested that too much synchronous activity diminishes information content (Chelaru and Dragoi 2008; Cohen and Kohn 2011). In addition, hypersynchrony can potentially trigger pathological brain states, as in epilepsy (McCormick and Contreras 2001). Although the definition and the time window of “synchronous” events varies depending on the context, it is clear that balancing the degree of neural coactivation, or network correlation, is crucial to maintain functional brain circuits.

The contributions of inhibitory interneurons to cortical activity have been extensively studied, as they are important building blocks of a cortical circuit, yet whether and how they contribute to information processing by populations of neurons still remains unclear. For example, parvalbumin positive (PV) interneurons, which comprise approximately 40% of cortical interneurons (Rudy et al. 2011), have been suggested to contribute to network synchrony (Cardin et al. 2009; Sohal et al. 2009). Also, although a contribution of PV neurons to visual recognition has been reported (Lee et al. 2012), the link between the underlying computation and PV-regulated network synchrony is largely unknown. This is partly due to the fact that previous studies focused only on the role of PV interneurons in regulating individual-cell outputs (Zhu et al. 2015), or bulk network oscillations detected by LFP recording (Cardin et al. 2009; Sohal et al. 2009). Recording from populations of neurons simultaneously with single cell resolution appears necessary to understand their role in information processing.

Based on previous finding that PV interneurons possess dense inhibitory connections to surrounding local pyramidal neurons (Packer and Yuste 2011), we hypothesized that this promiscuous innervation motif might serve to control neural synchrony and contribute to the spatio-temporal patterning of the neural population activity, affecting information coding. To explore this hypothesis and understand those spatial and temporal regulatory mechanisms more precisely, we used optogenetics to systematically suppress PV-cell activity while simultaneously performing two-photon Ca^{2+} imaging to record from large numbers of neurons with single-cell resolution, in mouse V1 in vivo. We specifically focused our analyses on the effects of PV-cell suppression on correlated activity (“neuronal ensembles”), to understand their functional contribution to visual information processing. We imaged both spontaneous and stimulus-evoked cortical activity, and analyzed those dynamics and the spatial extent of network synchrony. Our results provide evidence that PV neurons regulate network dynamics both temporally and spatially, and that they could contribute to implement information processing by making ensembles more distinct from each other.

Materials and Methods

Animals

All experimental procedures were carried out in accordance with Columbia University institutional animal care guidelines. Animals of both sexes were used, and were housed and maintained in a temperature-controlled environment on a 12-h light–dark cycle, with ad libitum food and water, in the Columbia University Animal Facility.

Virus Injection

Viruses were injected to PV-Cre mice (Jax: 008069) at the age of postnatal day (P) 20–30 for in vitro slice experiments, and P40–60 for in vivo experiments. Procedures were done as described previously (Atallah et al. 2012; Packer et al. 2012), with some modification. During surgery, mice were anesthetized with isoflurane (initially 2% (partial pressure in air) and reduced to 1%). A small circle (~1 mm in diameter) was thinned over the left V1 using a dental drill to mark the site for craniotomy to target the putative monocular region. AAV1/hSyn:GCaMP5G was obtained from the University of Pennsylvania Vector Core, while AAV1/CAG:Flex-ArchT-tdTomato and AAV1/CAG:Flex-tdTomato were developed by the Boyden lab and obtained from the University of North Carolina Vector Core. For in vivo experiments, either

AAV1/CAG:Flex-ArchT-tdTomato or AAV1/CAG:Flex-tdTomato was mixed with AAV1/hSyn:Flex-GCaMP5G at a 3:1 or 1:2 ratio, respectively, and injected into L2/3 of the left V1 over a 5 min period, at a depth of 200 μm from the pial surface, using a UMP3 microsyringe pump (World Precision Instruments). Two sites were injected (2.1 mm lateral to the midline, 0.0 or 0.7 mm rostral to lambda), and the total volume for each site was 175 nl or 75 nl, respectively. The beveled side of the needle was faced to the left so that viruses could be injected to and cover the V1 area of the left hemisphere. For the in vitro slice experiment, 200 nl of AAV1/CAG:Flex-ArchT-tdTomato was injected instead. We designed our injection protocol (especially volume and depth) carefully to minimize the virus infection in the deep cortical layer, because, as far as we know, excitatory PV neurons may exist there (Preuss and Kaas 1996).

Slice Preparation and In Vitro Optogenetic Experiments

At 2–3 weeks after the injection, 350- μm thick acute coronal slices were prepared from virus-injected mice using a Leica VT1200S vibratome after cardiac perfusion with ice-cold sucrose solution containing the following (in mM): 27 NaHCO_3 , 1.5 Na_2O_4 , 222 sucrose, 2.5 KCl, 3 MgSO_4 and 1 CaCl_2 . Slices were incubated at 36°C for 30 min in ACSF containing (in mM): 126 NaCl, 26 NaHCO_3 , 1.1 Na_2O_4 , 10 glucose, 3 KCl, 3 MgSO_4 and 1 CaCl_2 . During recordings, ACSF was similar except for (in mM): 2 MgSO_4 and 2 CaCl_2 . Sucrose and ACSF solutions were saturated with 95% O_2 and 5% CO_2 . Whole-cell recordings were made through 4- to 6-M Ω glass pipettes using Axon Multiclamp 700B amplifiers (Molecular Devices), digitized at 10 kHz with National Instruments 6259 multichannel cards and recorded using custom software written using LabView (National Instruments). Intracellular solution, pH 7.2, contained (in mM): 135 $\text{CH}_3\text{KO}_4\text{S}$, 8 NaCl, 10 HEPES, 2 Mg-ATP, 0.3 sodium-GTP, 7 phosphocreatine, and 10.7 biocytin. After ArchT-tdTomato expressing neurons were patched, a 617-nm LED (LUXEON Rebel LED, Luxeon Star LEDs) was placed under the slice chamber, the bottom of which was covered by a transparent glass, to assess the optogenetic manipulation of the patched neurons upon light illumination. LED illumination was performed in the middle of current injections or as a background during a series of current injections. Light intensity at the sample plane was approximately 17.6 mW/mm².

Immunohistochemistry

We performed immunohistochemistry as described previously (Pfeffer et al. 2013). Two to three weeks after the virus injection, the brain of the ArchT-tdTomato- and GCaMP-expressing mouse was extracted after perfusion with phosphate-buffered saline (PBS, pH 7.4) and following 4% paraformaldehyde (in PBS) under isoflurane anesthesia (2%), fixed in 4% paraformaldehyde at 4°C overnight, and sliced into 50 μm coronal sections. After the wash with PBS, free-floating sections were blocked with 1% BSA and 0.1% Triton X-100 in Tris-buffered saline (TBS) for an hour, and stained with primary antibody (1:1000 rabbit polyclonal anti-PV, Abcam, Ab11427) in the dark for at least 48 h at 4°C slowly shaking and with secondary antibody (1:500 goat antirabbit IgG conjugated with Alexa Fluor[®] 633, Invitrogen, A21070) at room temperature for 3–4 h in 0.5% BSA (TBS). Slices were mounted in Vectashield with DAPI (Vector Labs, H1500), and confocal images were obtained by a Nikon A1 and high N/A 60 \times water immersion objective lens (Plan Apo VC 60XWI, 1.20 N/A, Nikon).

Counting the number of overlapping cells between anti-PV and ArchT-tdTomato was also performed as described before (Pfeffer et al. 2013). In our specific case, because ArchT-tdTomato is localized to the plasma membrane and labels not only cell bodies but also dendrites and axons (Chow et al. 2010; Han et al. 2011), and because both pyramidal cells and PV cells are contacted and/or surrounded by other-neurons' ArchT-expressing axons and/or buttons, identification of soma of ArchT-expressing cells was difficult during *in vivo* two-photon microscopy (see Supplementary Fig. S1, upper panels). In contrast, the confocal-microscopy observation of brain slices after the immunohistochemistry procedures described above enabled us to identify slight but substantially characteristic signals from inside cell bodies, which frequently overlapped with anti-PV signals (see Supplementary Fig. S1, lower panels, and Supplementary Movie 2). We used this signal to count the number of ArchT-tdTomato expressing cells.

In Vivo Two-photon Imaging

In vivo two-photon imaging was performed as described previously (Miller et al. 2014), with some modifications. Briefly, 2–3 weeks after the virus injection, mice were anesthetized by urethane (1.1 mg/g body weight), and anesthesia was maintained by additional isoflurane (0.3–0.5%). A titanium head plate was attached to the skull using dental cement, and the cranial window was made around the virus injection site (1–2 mm in diameter) for the subsequent imaging. The activity of cortical neurons was recorded by imaging fluorescence changes with two-photon microscopy (Movable Objective Microscope; Sutter Instrument) and a Ti:sapphire laser (Chameleon Vision II; Coherent) at 950 nm, through a 20× water immersion objective (0.95 N.A.; Olympus). Also, a 1030 (or 1050) nm laser was used to distinguish ArchT-tdTomato (or tdTomato) signals from GCaMP5 signals. Scanning and image acquisition were controlled by Sutter software, MScan (4.07 frames per second for 512×512 pixels). During the imaging, light anesthesia was maintained by additional isoflurane (0.3–0.5%). Computations in V1 vary depending on brain state (Froudarakis et al. 2014). To minimize such experimental variables during our recordings, we anesthetized animals in the present study. During anesthesia, the brain is far from silent and a substantial amount of sensoricortical computation has been reported at the population level (Froudarakis et al. 2014). On the other hand, in awake mice, locomotion strongly modulates neural activity in V1 (Niell and Stryker 2010), suggesting that additional and variable inputs to V1 happen in the brains of awake mice.

In Vivo Electrophysiological Recording from PV Neurons

For the *in vivo* electrophysiological recording, animals were prepared as described in the imaging section above. After mounting the head plate as explained above, we performed *in vivo* whole-cell recording as described (Kitamura et al. 2008), or loose-patch recording as described (Atallah et al. 2012), in order to count the number of spikes during or without LED illumination. Briefly, under the guidance of the ArchT-tdTomato signals detected by two-photon microscopy, we targeted the PV neurons expressing ArchT-tdTomato. The surface of the brain was covered with 1.5% low-melting-point agarose dissolved in HEPES buffered saline containing (in mM): 150 NaCl, 2.5 KCl, 10 HEPES, 2 CaCl₂, 1 MgCl₂ (pH 7.3). A 4- to 6-M Ω glass pipette was filled with the intracellular solution described in the *in vitro* recording section, or with HEPES buffered saline, for the

whole-cell recording or for the loose-patch recording, respectively. During the recording, anesthesia was maintained by additional isoflurane (0.3–0.5%).

In addition to the targeted recording from PV-positive neurons, we also performed single-unit recording from multiple neurons simultaneously using multichannel microelectrode arrays, and identified putative inhibitory neurons as described previously (Barthó et al. 2004; Fujisawa et al. 2008). After preparing a 1×3 -mm window in the skull around the virus injection site, the dura was removed, and the probe was positioned so that the tips avoided large blood vessels. The recording silicon probe (NeuroNexus) was attached to a micromanipulator and inserted gradually to the target layer 2/3 of V1 (100–300 μ m depth from the surface of the brain). The probe consisted of 6 shanks (20- μ m shank separation), and each shank had 10 recording sites (20- μ m separation, 160 μ m² each site; 1–3 M Ω impedance). The wide-band neurophysiological signals were acquired continuously at 20 kHz on a 256-channel Ampliplex systems (KJE-1001, Ampliplex Ltd). Spike sorting was performed semiautomatically, using KlustaKwik2 (Kadir et al. 2014), followed by manual adjustment of the clusters. An autocorrelogram was also obtained to verify the cellular characteristics. Fast-spiking neurons were distinguished from regular-spiking neurons by a clustering method as described previously (Barthó et al. 2004).

Visual Stimulation and In Vivo Optogenetic Manipulation

Visual stimulation was performed as described previously (Miller et al. 2014). Visual stimuli were generated using the MATLAB (MathWorks) Psychophysics Toolbox (Brainard 1996) and displayed on a liquid crystal display monitor (19-inch diameter, 60-Hz refresh rate) positioned 15 cm from the right eye, roughly at 45° to the long axis of the animal. The 617-nm High-Power LED coupled to the \varnothing 400 μ m Core Patch Cable (Thorlabs) was positioned around the cranial window as described previously (Atallah et al. 2012). Light intensity at the tip was approximately 14 mW/mm². The tip was coupled to the fiber optic cannula (Thorlabs), and positioned under a 20× water immersion objective (0.95 N.A.; Olympus), to indicate the center of the imaging window. Overlap of the tip in the imaging field was avoided, and the distance between the cranial window and the tip was approximately 1.2 mm. The imaging setup, and the space between cranial window and the objective were completely enclosed with blackout fabric (Thorlabs). The left eye was also covered with blackout fabric or tape, to avoid visual inputs.

Mice were presented with sequences of full-field grating stimuli. Eight trials of different angles of the drifting gratings were performed in 1 session, and the order of presentations was alternated randomly at each session. The LED stimulation was delivered during every other visual stimulus, and the LED stimulation started 0.5 s prior to the onset of the visual stimulation, as described previously (Atallah et al. 2012) (see also Fig. 2A). Sine wave gratings (100% contrast, 0.035 cycles per degree, 2 cycles per second) drifting in 8 different directions were presented for 4 s, followed by 8 s of mean luminance gray screen. A total of 10 sessions were performed for each neural circuit (scanning plane), and the number of the trials of LED-on and LED-off were set to be equal at each angle of the drifting grating. The sequences of gratings were synchronized with image acquisition using Sutter software (MScan; Sutter Instrument).

Importantly, because over-suppression of inhibition can result in epileptiform or bursting network activity (Prince 1978; Connors 1984; Sanchez-Vives and McCormick 2000), and because too much stimulation of ArchT can cause rebound hyperactivation of ArchT-expressing cells (Mattis et al. 2012), a moderate range of inactivation of PV neurons was, in fact, deemed optimal for the present study. In a recent paper (Zhu et al. 2015), a strong optogenetic suppression of PV neurons caused epileptiform activity of pyramidal neurons. Authors of this work thus employed mild light illumination and found substantial optogenetic suppression of PV cells, and the level of pyramidal cell activation was very similar to our observations, suggesting that our manipulation was effective, but not pathological.

Recording During Spontaneous Activity

Spontaneous calcium signals were measured for ~13 min with the gray color displayed on the monitor, with room lights turned off. During this recording, the 4-s LED illumination for the optogenetics was performed with a 20-s interval, as described in Figure 2A. The number of trials for each circuit ranged between 10 and 20, and was typically 16.

Image Analysis

During periodic 617 nm LED illumination, GCaMP5 signals were detected via the band-pass emission filter 510/40 (Semrock). The raw images contained weak background increases. Considering the fact that neural activity is strongly correlated with $\Delta F/F$ (Akerboom et al. 2012; Peters et al. 2014), we postprocessed images and calculated $\Delta F/F$ with the following analyses. First, for frames during LED illumination, we calculated an “LED-on baseline” by measuring the median of signal intensities of all pixels at each frame, and then taking the median of all these values (excluding onset and offset frames of the LED). In the same way, a baseline during the 2.5-s period before LED onset was calculated as an “LED-off baseline” for each trial, and the difference between those two medians (LED-on baseline minus LED-off baseline) was calculated for each trial. This difference value was subtracted from LED-on frames so that the pixel-wise and cell-wise baselines during LED-on trials nearly matched the LED-off baselines immediately before it. The difference used for the subtraction was also used for the baseline subtraction of each onset and offset frame similarly, but in those cases, only the pixels showing a baseline increase, which could be clearly observed and detected by aligning all the pixels in each frame in the order of the scanning, were processed for the subtraction.

Those background-corrected images were then processed to correct brain motion artifacts using the enhanced correlation coefficient image alignment algorithm (Evangelidis and Psarakis 2008) or a hidden Markov model (Dombeck et al. 2007; Kaifosh et al. 2013). The regions of interest (ROIs) for the detection of neural activity were chosen using PCA/ICA based methods in MATLAB as described previously (Mukamel et al. 2009) (the code was kindly distributed by Dr Eran Mukamel), with some manual adjustment.

Further steps for the processing of GCaMP5 signals to detect signal change $\Delta F/F$, were performed as described previously (Peters et al. 2014). The MATLAB code to subtract fluctuations of the background fluorescence before calculating $\Delta F/F$ was kindly provided by Dr Komiyama (Peters et al. 2014), and was used with some modification. Briefly, a ring-shaped “background ROI” was created for each ROI 2–5 pixels away from the

border of each neuronal ROI to a width of 30–35 pixels, and the size was adjusted in order to contain at least 20 pixels in each background ROI after all the following steps. From the background ROI, we removed the pixels that belonged to any neuronal ROIs, and the ones that contained artificially added pixels (added black pixels at the edge of the image as a result of the motion correction procedure) at any time point. Then we removed the pixels that, at some time point(s), showed signals exceeding that of the neuronal ROI by two times the standard deviation of the difference between each background ROI pixel time series and the neuronal ROI time series. The resulting background ROI signals were averaged at each time point, and a moving average of the time series was calculated. Using the moving average instead of the raw background ROI signal was helpful to minimize the production of an artificially large increase or decrease at each time point as a result of the subtraction, which could have altered the analyses of the timing of neural activations. Pixels within each neuronal ROI were also averaged to give a single time course, and then the background ROI signal was subtracted. Then $\Delta F/F$ of GCaMP5 signals of all neurons in each circuit were calculated.

To quantify neuronal activity, we measured $\Delta F/F$ of GCaMP5 signals (Akerboom et al. 2012; Peters et al. 2014) during visual stimulation, with or without LED stimulation (Fig. 2B,C; see also Methods). For some analyses, spike probabilities were also inferred from the $\Delta F/F$ (see Supplementary Fig. S3A–E) as an alternative estimate of neuronal activation, but for maximum alignment with previous work (Hofer et al. 2011a) in which $\Delta F/F$ data was used directly for the analyses of temporal dynamics of a neural population, we mainly used $\Delta F/F$ data for subsequent analyses. Neurons with noisy signal with no apparent calcium transient were detected by visual inspection and excluded from further analysis.

Spike probability was inferred from calcium signals $\Delta F/F$ using a fast, nonnegative deconvolution method as described previously (Vogelstein et al. 2010). As for the parameters used in the calculation, the decay constant of calcium transients, τ , was set to 1.3 s, and the P. lam was set to 0.07.

Statistical Analysis

We used MATLAB for statistical analyses. Wilcoxon signed rank tests was mostly used to determine statistical significance ($P < 0.05$) unless otherwise indicated. All P values less than 0.0001 were described as “ $P < 0.0001$ ”.

Data Analysis

For data analyses of the spontaneous activity, signals during LED illumination (for 4 s) were compared with those before the LED onset using the same number of frames. For the analyses of the visually evoked activity, signals acquired during the visual stimulation delivered together with the LED stimulation (for 3.5 s as shown in Fig. 2A) were compared with the signals during visual stimulation without LED illumination by using same number of frames. Nonvisually responsive cells were excluded from further analysis as described previously (Hofer et al. 2011b), by testing whether, for each cell, a significant calcium response during LED-off was observed relative to baseline for at least one grating direction (one-way ANOVA). Since excitatory cells, which we analyzed in the present study as described below, do not express ArchT, we considered cells showing lower average activity to all drifting gratings during LED illumination than the baseline

activity as nonvisually responsive cells. In both cases, LED-onset and -offset frames were excluded from the analyses.

To analyze the orientation tuning curve and related parameters (OSI, DSI, and HWHH), the average $\Delta F/F$ was taken as the response to each grating stimulus. For the peri-stimulus time histogram (PSTH), the LED onset frame was set as a zero time point. Visually evoked responses during LED-on or LED-off were separately averaged, and used for further analyses, as described previously (Hofer et al. 2011a; Atallah et al. 2012; Miller et al. 2014). Briefly, preferred orientation was taken as the modulus of the preferred direction to 180° . Orientation selectivity index (OSI) was calculated as $(\text{Resp}_{\text{best}} - \text{Resp}_{\text{ortho}}) / (\text{Resp}_{\text{best}} + \text{Resp}_{\text{ortho}})$, where $\text{Resp}_{\text{best}}$ is the response at the preferred direction and $\text{Resp}_{\text{ortho}}$ is the average of responses to the directions orthogonal to the best direction. The direction selectivity index (DSI) was calculated as $(\text{Resp}_{\text{best}} - \text{Resp}_{\text{null}}) / (\text{Resp}_{\text{best}} + \text{Resp}_{\text{null}})$, where $\text{Resp}_{\text{null}}$ is the response at 180° away from the best direction. Cells with an OSI < 0.4 (calculated without LED illumination) were considered to be unselective for orientation. Most of the inhibitory neurons in V1 possess a lower OSI than excitatory ones, which means less selectiveness to the most-preferred orientation of visual stimulation. Since most inhibitory neurons have OSIs of less than 0.4 (Sohya et al. 2007; Kerlin et al. 2010), we removed OSI-low cells (< 0.4) for the analyses, unless otherwise indicated, in order to remove the potential contamination of inhibitory neurons. Responses to the 8 grating directions were fit with orientation tuning curves, i.e., a sum-of-Gaussians (see Supplementary Fig. S4). The double Gaussians are forced to peak 180° apart, and to have the same tuning sharpness (σ) but can have unequal height, with a constant baseline B. For the fitting, standard error for each angle was used together with the average to estimate the initial parameters and perform the further fitting to calculate parameters more accurately. The tuning sharpness was measured as $\sigma (2 \ln(2))^{1/2}$, i.e., the half-width at half height (HWHH).

Change in the activity was assessed by directly comparing the difference of the activity (average of $\Delta F/F$ per second) between the LED-on and LED-off condition, or by using an “activity index” to consider the degree of the change. Activity index was calculated by $(\text{Act}_{\text{on}} - \text{Act}_{\text{off}}) / (\text{Act}_{\text{on}} + \text{Act}_{\text{off}})$ where Act_{on} is the activity ($\Delta F/F$) during LED-on and Act_{off} is the activity during LED-off (in the case of spontaneous activity, the Act_{off} was the activity immediately “before” the LED-on period). $\Delta F/F$ not often but sometimes took a negative value, and $(\text{Act}_{\text{on}} + \text{Act}_{\text{off}})$ could be zero. In that case, to calculate the activity index, the smaller value between Act_{on} and Act_{off} was used as a baseline, and the baseline was subtracted from both Act_{on} and Act_{off} and then the activity index was calculated (as a result, the value became either -1 or 1). In that case, to consider the effect of LED illumination statistically, the average of $\Delta F/F$ during LED-on and that during LED-off were compared by Wilcoxon signed rank test. A one-sample t-test was also used to consider the activity change (whether the difference between Act_{on} and Act_{off} was significantly different from zero), as shown in Supplementary Fig. S3H, I.

To evaluate the effect of LED illumination on the coactivation of neural activity, which we call “total correlation” in the present study, we calculated pairwise correlations using Pearson’s correlation coefficient, from the GCaMP5 signals ($\Delta F/F$) of two cells over the duration of LED-on and LED-off, and they were compared statistically. To consider the timing of each activity, raw traces of each neuron were not averaged but instead concatenated, and used for the calculation. Then the calculated correlation coefficients were statistically analyzed. We also

performed analyses based on surrogate datasets, as described in the previous work (Miller et al. 2014). We generated 1000 independent surrogate datasets by randomizing the order of the signals ($\Delta F/F$) within each cell (shuffling within cells), using concatenated raw traces, so that the timing of the activity was randomized while the total activity of each cell was preserved. Using them, 1000 correlation coefficients for each pair were obtained, and the mean response of each pair was used for the further statistical analyses.

To investigate the role of PV neurons in regulating the response reliability of multineuronal activity, we measured correlation coefficients between population activity patterns at different frames (or time points) to calculate “frame–frame correlation” that represents ensemble similarity. Given that different visual information is assumed to be encoded by different neuronal ensembles, larger frame–frame correlation between ensembles during different visual stimuli (different angles of drifting gratings) means lower stimulus discrimination performance. We compared frame–frame correlation at different states (i.e., LED-off or LED-on) to evaluate the role of PV neurons in the regulation of stimulus-discrimination performance by the multineuronal activity.

As described previously (Miller et al. 2014), a neuronal ensemble was defined by coactivation of a group of neurons in a high-activity frame, and the similarity between ensembles was evaluated by calculating the Pearson’s correlation coefficient between ensembles. Here, raw $\Delta F/F$ data were directly thresholded to a level of 4 SDs above 0 and used to define coactive frames in the present study (we tested 2, 3, 4, 5 SDs and observed the same effect of PV-cell suppression). As performed previously (Miller et al. 2014), frame–frame correlation was calculated without excluding nonvisually responsive neurons to avoid repeated thresholding of data, while we also observed a similar effect of PV-cell suppression when they were excluded. Circuit-by-circuit analysis (see Supplementary Fig. S5 and 7) was also performed by calculating the mean response of each circuit.

To investigate the relationship between cell–cell correlation (total correlation) or neuronal activity, and frame–frame correlation, we calculated the mean response of each circuit, and analyzed tendencies of overall observed circuits ($N = 8$ of the PV-ArchT animals) by measuring Pearson’s correlation coefficient and statistical significance (P values) between those parameters. The role of PV cells was also evaluated by analyzing changes in those parameters driven by PV-cell suppression.

Relationships between total correlation and distances between pairs of neurons were also considered. The correlation coefficients of all pairs were separated into 8 categories depending on the distances between them: ~ 50 (i.e., more than 0, and less than or equal to 50), ~ 100 (i.e., more than 50, and less than or equal to 100), ~ 150 , ~ 200 , ~ 250 , ~ 300 , ~ 350 , and $\sim 400 \mu\text{m}$, as shown in Figure 4. Because number of pairs of more than $300 \mu\text{m}$ distance was only about 1% among all pairs, we used the pairs of 0– $300 \mu\text{m}$ distance for the analyses in this study. The effect of the LED illumination (LED-off vs. LED-on) was evaluated statistically by Wilcoxon signed rank test, at each category, for each condition (visually evoked activity or spontaneous activity).

LFP Recording and Analysis

For in vivo recording of LFPs in mice, an AgCl-electrode in a glass pipette filled with saline solution was inserted into approximate layer 2/3 ($250 \mu\text{m}$ below the surface) in V1 and referenced to an AgCl-wire surgically inserted onto superficial

ipsilateral cerebellum. In order to maximize the number of trials (>100 total collected) and thus the signal-to-noise ratio, we minimized the duration of the experiment during the visual stimulation portion by utilizing a slightly shortened stimulus duration (3 s or 1 s) and interstimulus interval (6 s).

LFP data were manually prescreened for excessive artifacts (e.g., signal greater than 8 standard deviations, or obvious breathing or muscle related artifact) and deviant trials were removed (<10% of trials). The shortened timescale was more than adequate to capture stimulus-elicited oscillations since spectral power returned to baseline levels by 2000 ms poststimulus onset (see Supplementary Fig. S2E–G). LFPs were segregated into bins –1000 ms pre to 5000 ms postgrating stimulus onset. Data were convolved with a family of modified Morlet wavelets ranging from 2 to 100 Hz in 1 Hz and 20 ms steps with wavelet size increasing linearly from 1 to 20 cycles using code written in MATLAB and EEGLAB 9.0 (Delorme and Makeig 2004). This approach optimizes effective frequency resolution at low frequencies and time resolution at higher frequencies (Hamm et al. 2012). Oscillatory power was expressed in decibels, or 10 times log₁₀ of the instantaneous absolute-value of the complex wavelet result divided by the average absolute value across the baseline period: –1000 to –600 ms pregrating onset. For statistical comparison, power was averaged across the first 1000 ms postgrating onset (since this was when the majority of the response was present, see Supplementary Fig. S2E–G) separately for each frequency bin and compared within animals between LED-on and LED-off trial averages with paired-samples *t*-tests (*df* = 3).

Results

Optogenetic Inactivation of PV Neurons with Simultaneous Two-photon Ca²⁺ Imaging In Vivo

To genetically and optogenetically control the activity of PV neurons in a region-specific and subtype-specific manner, we used a gene expression system based on the adeno-associated virus (AAV) with PV cell-specific Cre transgenic mice (Atallah et al. 2012). ArchT, which enables the hyperpolarization of ArchT-expressing neurons upon illumination with specific wavelengths (Chow et al. 2010; Atallah et al. 2012), was specifically expressed in the PV interneurons in V1, so that their activities were temporarily and reversibly inactivated during the light illumination. To visualize ArchT expression, we used a construct encoding ArchT fused with tdTomato (ArchT-tdTomato).

An AAV encoding GCaMP5, a genetically encoded calcium indicator (Akerboom et al. 2012; Peters et al. 2014), was simultaneously injected to monitor the activity of multiple neurons with single-cell resolution using two-photon microscopy (see Supplementary Movie 1). GCaMP5 fluorescent signals were distinguishable from the ArchT-tdTomato signals based on their different emission spectra (Fig. 1A; see Supplementary Fig. S1 upper panels). We almost never detected GCaMP5 signals from tdTomato-positive neurons, even though GCaMP5 expression was regulated by the human synapsin one gene (*hsyn*) promoter and thus is normally expressed in all neuron types. Considering that 80% of neurons in the cortex are excitatory, and that the activity of PV neurons, the largest subtype of cortical interneurons (Rudy et al. 2011), were not typically labeled with GCaMP5 in our experiments, we assumed that most of the imaged neuronal activity arose from excitatory pyramidal neurons.

After maturation of AAV-driven expression, mice were placed under a two-photon microscope for imaging (Fig. 1B). To image GCaMP5 signals during optogenetic stimulation, a band-pass

emission filter 510/40 was used for detection, and a 950-nm laser was used for the two-photon excitation of GCaMP5. A 617-nm LED was used for the optogenetic manipulation to avoid overlap with the detection wavelength window. This wavelength suppressed neuronal activity in PV cells expressing ArchT-tdTomato in vitro (see Supplementary Fig. S2A and B) as expected from its broad-action spectrum (400–650 nm) (Chow et al. 2010).

This optogenetic suppression of PV neurons was also confirmed in vivo. Though the ArchT-expressing neurons rarely showed GCaMP5 signals, we did identify one PV neuron labeled with both (Fig. 1C). The spontaneous activity of this cell was recorded with or without LED illumination repeatedly (Fig. 1D), and we found that the activity significantly decreased during LED illumination ($P < 0.01$, $df = 2$, $F = 5.77$ one-way factorial ANOVA; further post hoc Tukey–Kramer test showed a significant difference between “before-LED” and “during-LED” ($P < 0.01$), and between “during-LED” and “after-LED” ($P < 0.05$), but not between “before-LED” and “after-LED” ($P = 0.99$) (Average $\Delta F/F$ of GCaMP5 signals (Akerboom et al. 2012; Peters et al. 2014) per second and s.e. for each condition; “before-LED”, 5.12 ± 0.77 (%); “during-LED”, 1.95 ± 0.53 ; “after-LED”, 4.97 ± 0.89).

Electrophysiological recording from PV neurons in vivo also showed a similar tendency (Fig. 1E–G; see Supplementary Fig. S2C, D). All recorded PV neurons ($n = 3$) showed a decreased spontaneous firing rate during LED illumination (see Supplementary Fig. S2C, D; average firing rate (spikes per sec) and s.e. was 4.15 ± 2.00 , or 2.91 ± 2.16 , for “Before LED” or “During LED,” respectively). This observed effect is consistent with a previous report of a 30–40% decrease in spontaneous activity in PV neurons during optogenetic inactivation using ArchT (Atallah et al. 2012). Since the impact of PV cell suppression varied (see Supplementary Fig. S2D), we further performed in vivo recording using multichannel microelectrode arrays and used the following analyses to identify putative inhibitory neurons (Barthó et al. 2004), to evaluate the general trend of our optogenetic manipulation (Fig. 1E–G). We identified putative inhibitory neurons as those showing clear suppression of their activity during LED illumination (an example is shown in Fig. 1E,F). Statistical analyses of all recorded putative inhibitory interneurons revealed that they were indeed significantly inactivated by LED illumination (Fig. 1G). Considering that 30–50% of inhibitory neurons are PV-positive interneurons in layer 2/3 of V1 (Gonchar et al. 2007), and that most of the PV cells expressed ArchT as shown below, the activity index (–26%) suggests that most of the PV interneurons were moderately and significantly suppressed during the LED illumination in vivo.

We also evaluated the impact of our optogenetic suppression of PV cells using a histological method and electrophysiological recording from the bulk of neurons (local field potential [LFP] recording). ArchT is a protein that localizes to the cellular membrane (Chow et al. 2010; Han et al. 2011), and both pyramidal cells and PV cells were contacted and/or surrounded by axons or buttons of other ArchT-expressing PV cells, as indicated previously (Pfeffer et al. 2013). Thus, it was difficult to identify the number of ArchT-expressing neurons during in vivo two-photon imaging, and only cells with a very high expression level could be identified (Fig. 1A; see Supplementary Fig. S1 upper panels). On the other hand, immunohistochemistry and subsequent observation by confocal microscopy with a higher N/A objective lens (1.20N/A, Nikon) enabled us to confirm the specificity of ArchT expression in PV neurons (see Supplementary Fig. S1, lower panels; Supplementary Movie 2). We found that more than 85% of PV neurons expressed ArchT-tdTomato, suggesting that almost all of the PV neurons were potentially under optogenetic

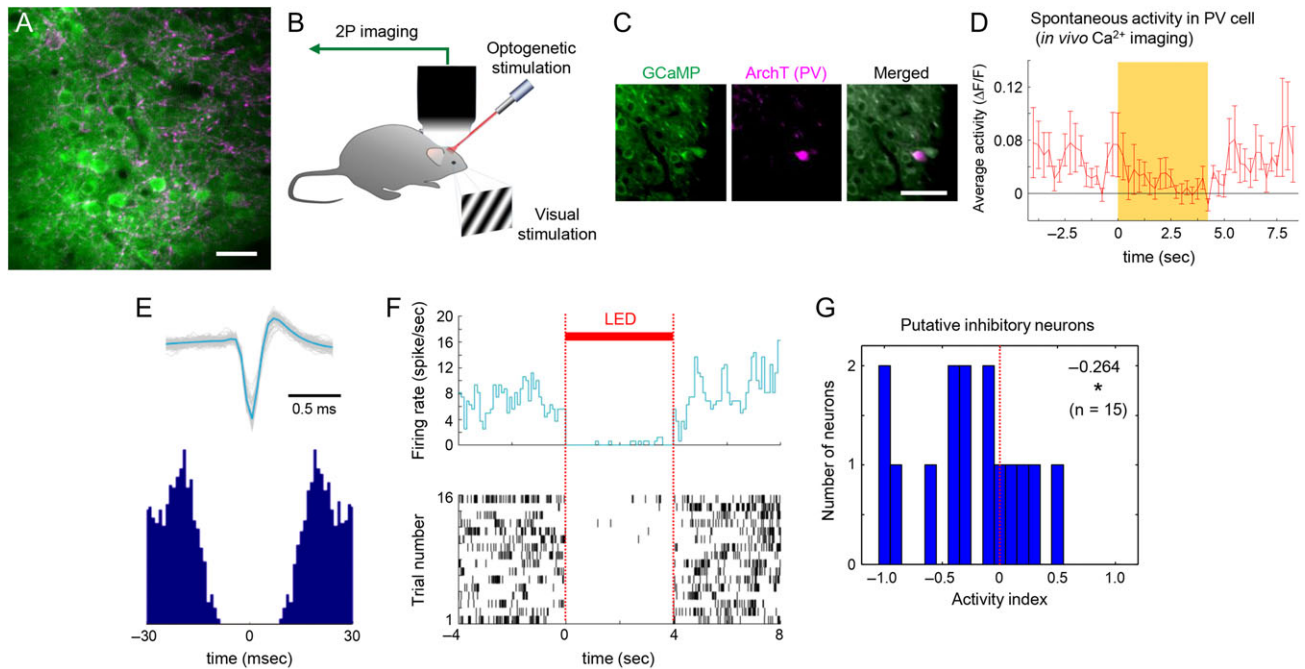


Figure 1. Imaging neuronal activity with and without optogenetic suppression of PV neurons. (A) Example of expression pattern of GCaMP5 (green) and ArchT-tdTomato (magenta), induced by AAV vectors coinjected into L2/3 in mouse V1. Multiple cell bodies of GCaMP5-expressing neurons were surrounded by fibers and synaptic boutons from ArchT-expressing PV neurons. Scale bar, 25 μm . (B) Setup for optogenetic manipulation during *in vivo* two-photon Ca^{2+} imaging. The right eye of the mouse was presented with a gray screen (for spontaneous activity) or drifting gratings (for visually evoked activity), whereas the left eye was covered completely by a blackout fabric to avoid visual inputs from the screen or LED light. (C) A PV neuron showing both strong expression of ArchT-tdTomato and Ca^{2+} signals *in vivo*. Scale bar, 50 μm . (D) Activity change of the PV cell expressing ArchT *in vivo*. Time course of mean activity over 30 trials. Spontaneous activity detected by GCaMP signals was significantly suppressed during the LED illumination. Yellow, LED illumination; error bar, s.e. (E) An example of a putative inhibitory interneuron in a PV-ArchT animal. This cell showed a typical spike waveform, when considering “half-amplitude duration” and “trough to peak time” (upper panel). An autocorrelogram of this cell (lower panel) suggested a high frequency of spikes during the normal (LED-off) condition (approximately ~ 50 Hz), typical of PV neurons. (F) The average firing rate (upper panel) and raster plot of the activity over 16 trials recorded from the same cell in panel E showed that this cell was clearly inactivated during the LED illumination, confirming the effect of the ArchT. (G) Summary of changes in activity of all observed putative inhibitory neurons (from 3 PV-ArchT animals). An “activity index” was used to quantify the change in activity by LED illumination. Average, P value (one-sample t -test was performed to consider whether the value was significantly different from zero), and total number of observed neurons are shown in the panel respectively. LED, timing of LED illumination; *, $P < 0.05$.

manipulation during our experiments. We also performed LFP recordings from the animals expressing ArchT in PV cells, and confirmed an expected (Cardin et al. 2009; Sohal et al. 2009) decrease in stimulus elicited oscillatory power specific to the gamma-band (see Supplementary Fig. S2E–G). These findings strongly support the efficacy of our optogenetic manipulation of PV neurons and also indicated their potential role in the regulation of high frequency cortical synchrony.

Optogenetic Suppression of PV Cells During Visual Stimulation Increases Neuronal Activity

We then compared results from PV-ArchT expressing animals with those from control animals (animals expressing tdTomato instead of ArchT, as explained below), to investigate the specific role of PV neurons in regulating the dynamics of the local network.

Neuronal activity was imaged simultaneously from multiple neurons in layer 2/3 of V1 during visual stimulation or during spontaneous activity, and the effect of the PV-cell suppression was investigated across these two conditions (Fig. 2). To quantify neuronal activity, we measured the $\Delta F/F$ of GCaMP5 signals (Akerboom et al. 2012; Peters et al. 2014) during visual stimulation, with or without LED stimulation (Fig. 2B,C; see also Methods). We used $\Delta F/F$ for subsequent analyses, instead of inferred spike

probabilities (see Supplementary Fig. S3), for greater consistency with previous work (Hofer et al. 2011a).

Although most of the imaged cells were likely excitatory (as explained in the Materials and Methods), the possibility still remained that they might contain some inhibitory neurons. Thus, for the following analyses, we computationally removed putative inhibitory neurons by calculating the OSI (Sohya et al. 2007; Kerlin et al. 2010), unless otherwise indicated.

We then characterized the effects of the suppression of PV neurons on visually evoked activity. During LED illumination, neural activity was slightly but significantly increased in animals in which PV neurons expressed ArchT-tdTomato (PV-ArchT animals) (Fig. 2D,E). We compared these results with those of control animals, where PV neurons in V1 only expressed tdTomato instead of ArchT-tdTomato, and confirmed that PV-cell suppression significantly “increased” neural activity (Fig. 2E,F). The increased neural activity by PV-cell suppression was observed in both $\Delta F/F$ and computationally inferred spike probabilities analyses (see Supplementary Fig. S3A–E). The increase in overall activity by the PV-cell suppression was also present even when all the recorded neurons, including ones of lower OSI (< 0.4), were used for the analyses (see Supplementary Fig. S3F–I). We also found no bias caused by differences in basal fluorescence levels (see Supplementary Fig. S3J–M). These results are consistent with previous electrophysiological single-unit recordings performed together with optogenetic suppression of PV neurons by ArchT

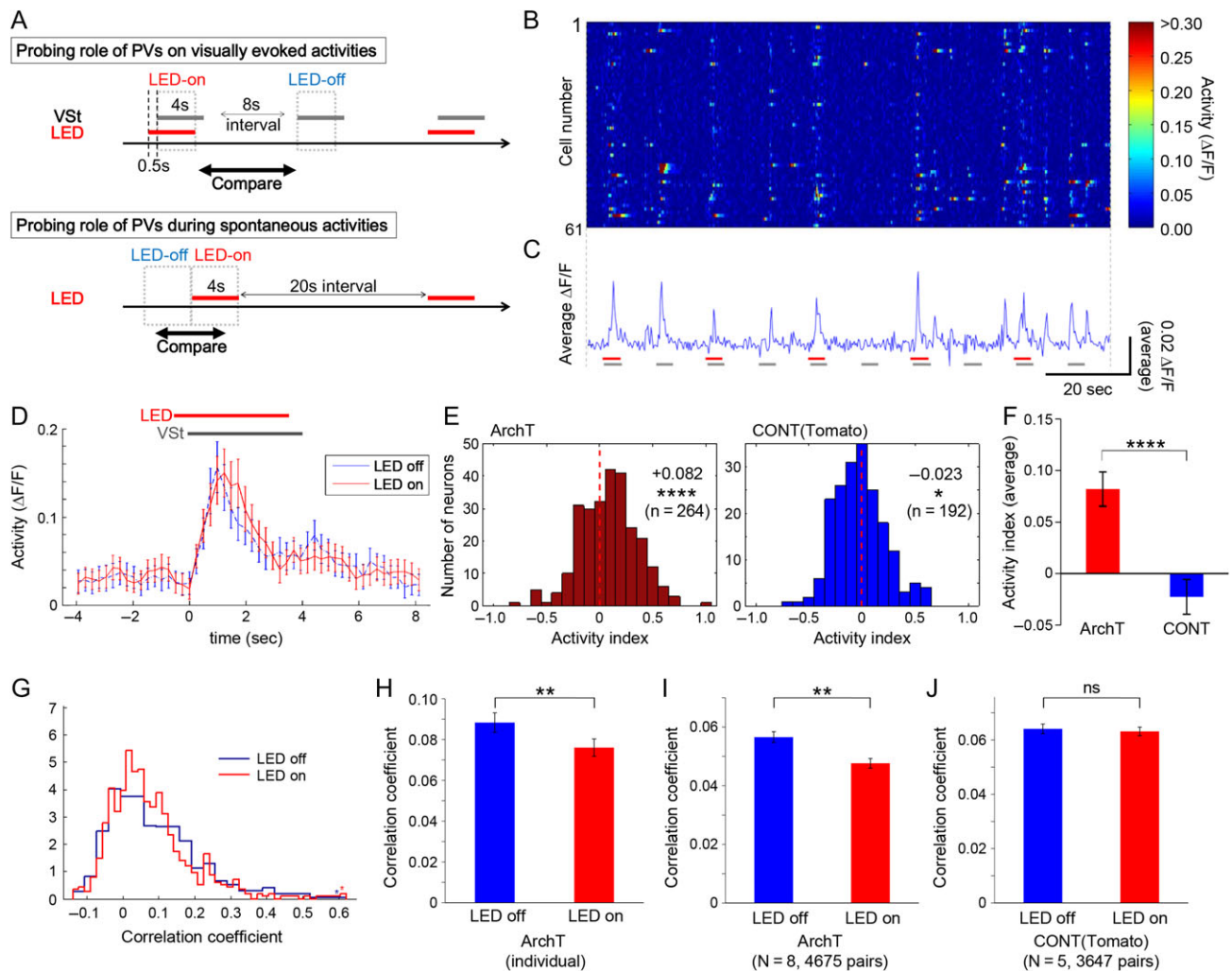


Figure 2. Inactivating PV neurons decreases network-wide synchrony. (A) Experimental procedures during visually evoked (upper panel) and spontaneous (lower panel) activity. Drifting gratings (8 different directions in each session, at random order) were used as visual stimulation, and LED illumination (4 s stimulus and 20 s interval LED) was used for optogenetic stimulation. VSt, timing of visual stimulation. (B, C) An example of time course changes of activities in simultaneously recorded multiple neurons ($n = 61$), with repeated visual stimulations (gray bar), and with or without LED stimulation (red bar). Neural activity was calculated from GCaMP5 signal, and plots of individual cells (B) and their average $\Delta F/F$ (C) depict visually evoked responses as well as spontaneous activations in the inter-trial interval. $\Delta F/F$ data were used for subsequent analyses, except when inferred spike probability was also tested (see Supplementary Fig. S3A–E). (D) Average activity traces over all trials across all 61 cells from the circuit shown in B, and C are plotted, showing a small increase in activity during LED illumination. LED, timing of LED illumination; VSt, timing of visual stimulation. (E) Summary of changes in activity of all observed networks ($N = 8$ circuits from 6 PV-ArchT animals (left), and $N = 5$ from 3 PV-Tomato animals (right)). An “activity index” was used to quantify the change in activity by LED illumination. Results of comparisons between “LED off” and “LED on” are shown in each panel (average, P value (Wilcoxon signed rank test), and total number of observed neurons, respectively). (F) The activity increase driven by PV suppression was also proved significant when compared with PV-Tomato control animals (same data in (E) were analyzed by Wilcoxon rank sum test). (G, H) LED illumination induced significant decorrelation in an example neural circuit (the same circuit shown in panel B–D). Histogram showing distributions (G) and bar graph showing averages (H) of correlation coefficients, which were computed from all neuronal pairs in the circuit, suggest significant decreases in a PV-ArchT animal during LED illumination. Starred column, the bin for all values that lie off the edge of the graph. (I, J) Summary of effects of LED illumination on correlated neural activity. PV-ArchT animals (I, $N = 8$ and 4675 pairs) showed a significant LED-induced decrease, while control animals (J, $N = 5$ and 3647 pairs) showed no significant change. Error bar, s.e.; ns, not significant; * $P < 0.05$; ** $P < 0.01$; **** $P < 0.0001$.

(Atallah et al. 2012; Zhu et al. 2015), showing a significant increase in neural activity during visual stimulation. This also supports that our optogenetic manipulation was adequate to disrupt the PV-cell activity and study their functional impact on the network.

We further confirmed that our experimental conditions and the effect of the PV-cell inactivation were consistent with those of previous studies (Ohki et al. 2005; Ko et al. 2011; Atallah et al. 2012) (see Supplementary Fig. S4). Without LED illumination, the map of the orientation preferences in mouse V1 showed a typical “salt and pepper” distribution (see Supplementary Fig. S4B) (Ohki et al. 2005; Ko et al. 2011). The distribution of OSI values in our data was

similarly random (see Supplementary Fig. S4C). During LED illumination in PV-ArchT animals, the distribution of changes in the OSI was also spatially random (see Supplementary Fig. S4D). On the other hand, the OSI was decreased by the optogenetic inactivation of PV cells (see Supplementary Fig. S4E). The DSI was also “decreased” by PV-cell inactivation (see Supplementary Fig. S4F). The half-width at half height (HWHH), which reflects the sharpness of the tuning within cells, was not significantly changed by the suppression of PV neurons (see Supplementary Fig. S4G). Recent reports suggest that testing various strengths and durations of optogenetic manipulation is necessary to show conclusive

results regarding the role of PV neurons in orientation tuning (Atallah et al. 2014; El-Boustani et al. 2014; Lee et al. 2014), however, the consistency of our orientation tuning results with those of a previous report (Atallah et al. 2012) further support the reliability of our method in the present investigations.

Optogenetic Suppression of PV Cells During Visual Stimulation Decreases Neuronal Synchrony

To evaluate the effect of the PV-cell suppression on neuronal coactivations, we measured the correlation coefficients between activity traces from pairs of neurons, for neurons within a single two-photon scanning plane, as described in Methods. Our approach of concatenating trials prior to calculating correlation coefficients served to estimate the cross-trial interdependence and activity onset similarity between neuronal pairs. This type of pairwise time-varying correlation, which we call “total correlation”, as previously defined (Hofer et al. 2011b), was significantly decreased by the suppression of PV neurons in an example group of neurons, and a systematically shifted distribution with lower correlations was observed (Fig. 2G,H). A significant decrease in pairwise time-varying correlations was observed even when all results from multiple experiments were combined (Fig. 2I), while data from the control animals did not show any significant change during the LED illumination (Fig. 2J). The effect of the PV-cell suppression was consistently verified even by the circuit level analysis (see Supplementary Fig. S5A).

We further performed analyses based on surrogate datasets, following the method described in previous work (Miller et al. 2014). Total correlations calculated from the surrogate datasets (during visual stimulation, shuffling within each cell before the calculation, 1000 times shuffling) were much closer to zero comparing with the actual data shown in Figure 2I, irrespective of LED-on/off ($0.51 \times 10^{-5} \pm 2.09 \times 10^{-5}$ (mean and s.e.) for LED-off, $n = 4675$ pairs, $P = 0.8072$ (one sample t-test to consider the difference from zero); $-1.69 \times 10^{-5} \pm 2.07 \times 10^{-5}$ for LED-on, $n = 4675$ pairs, $P = 0.4146$ (one sample t-test)). Total correlations calculated from the surrogate datasets were also significantly smaller than the actual data, irrespective of LED-on/off ($P < 0.0001$ in both cases, Wilcoxon signed rank tests). These results support that the values we observed in actual total correlation reflect the actual neuronal coactivity. Also, when analyzing the total correlations calculated from the surrogate datasets, there was no significant difference between LED-off and -on ($P = 0.7020$, 4675 pairs, Wilcoxon signed rank tests), suggesting that significant change in actual total correlation we observed (Fig. 2G–I) reflects the true change in the network coactivity. Furthermore, since shuffling does not change the total activity of each neuron, these results suggest that activity increase caused by the PV-cell suppression (Fig. 2D–F) is unlikely a causal factor of the decreased total correlation (Fig. 2G–I).

These results suggest that PV cells control and promote stimulus-driven coactivation among excitatory neurons. Although more spikes are generated by the network during PV-cell suppression, these spikes are less correlated. Our result is consistent with the previous observation in vivo that PV neurons regulate network correlations (Cardin et al. 2009; Sohal et al. 2009), though at a different time scale.

Suppression of PV Cells also Decreases Spontaneous Correlations

In our experiments, cortical neurons were spontaneously active, even without visual stimulation as shown before (Hofer

et al. 2011a; Miller et al. 2014). Since there is absent or greatly reduced specific input from the retina via thalamus during spontaneous activity, we sought to compare the effect of PV-cell suppression on activity levels and overall network synchrony during spontaneous activity to the effects found during visual stimulation. This may help discern the contribution of input specificity and circuit connectivity.

During spontaneous activity, neuronal activity was not significantly changed by the LED illumination in PV-ArchT animals (Fig. 3A), consistent with a previous electrophysiological observation (Atallah et al. 2012). Basal fluorescence levels did not influence the activity of the neurons or the effect of LED illumination (see Supplementary Fig. S6A, B).

In contrast, total correlation significantly decreased during LED illumination in the PV-ArchT animals (Fig. 3B; see Supplementary Fig. S5B). Analysis with inferred spike probabilities also showed a similar effect during spontaneous activity ($P < 0.01$). The consistent effects of PV-cell suppression during both spontaneous activity and visually evoked activity supports the role of PV neurons in the regulation of the network coactivation and also the dependence of the regulatory mechanism on the intrinsic functional connectivity between postsynaptic cortical neurons, rather than on the stimulus-activated connectivity. In addition, because there was no significant increase of spontaneous activity during PV-cell suppression, these results indicate that the regulation of the network correlation by PV neurons can be independent of firing rate of the neural network.

PV Neurons Enhance Spatial Extent of Network Coactivation

Two-photon imaging of neural activity has allowed unprecedented insight into circuit function due to its high spatial resolution (Ohki et al. 2005, 2006; Ko et al. 2011; Hofer et al. 2011a; Atallah et al. 2012). To exploit this advantage, we investigated the functional contribution of PV cells to the spatial regulation of neural network synchrony and dynamics.

First, we investigated the spatial extent of pairwise correlations between neurons. During visual stimulation with the LED off, total correlation was higher at smaller distances between neuronal pairs (Fig. 4A). Interestingly, when we investigated the effect of PV cell suppression, we found that the decrease in total correlation was significant only when the distance between neuronal pairs was less than $150 \mu\text{m}$ (Fig. 4A,B). A previous study (Packer and Yuste 2011) demonstrated that PV neurons possess dense inhibitory connections to excitatory neurons, especially

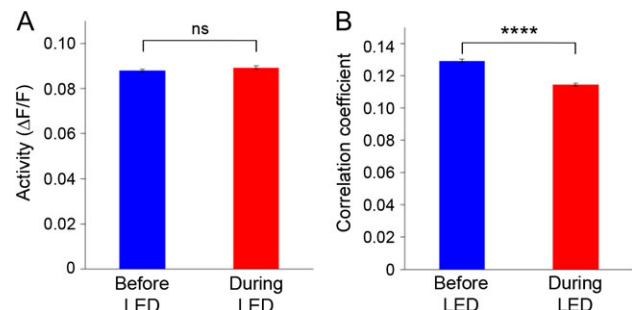


Figure 3. The effect of PV-cell suppression during spontaneous activity. (A) During spontaneous activity, neural activity was not significantly changed by LED illumination in PV-ArchT animals ($N = 7$, 501 neurons). (B) In contrast, PV-cell suppression significantly decorrelated spontaneous neural activity ($N = 7$, 18 328 pairs).

those within 150–200 μm in cortical layer 2/3. We therefore reasoned that the optogenetic suppression of PV neurons might mainly affect local correlations maintained by the common or shared inputs from PV neurons.

Similarly, the total correlation during spontaneous activity was also affected by PV-cell suppression in a distance-dependent manner (Fig. 4C,D), suggesting that distance-dependent regulation may be preserved, irrespective of the network state or the synaptic inputs to layer 2/3 in V1. Altogether, these results indicate that a spatial gradient of neural synchrony is likely to be maintained and/or enhanced by PV interneurons via intrinsic anatomical connections.

PV Suppression Enhances Ensemble Similarity

Based on our findings that PV interneurons can control the spatio-temporal patterning of neuronal synchrony, we hypothesized that PV interneurons might also regulate multineuronal information processing through the regulation of spatially distributed population activity patterns. Two-photon microscopy is actually a useful tool for investigating the regulatory mechanism of neuronal ensembles, patterns of multineuronal activities, because it enables recording from a large population of individual neurons simultaneously (Cossart et al. 2003). We investigated the role of PV neurons in the regulation of multineuronal activity by comparing evoked population activity patterns during different visual stimuli (different angles of drifting gratings). We

measured correlation coefficients between population activity patterns at each frame (or time point) to calculate “frame–frame correlation” that represents ensemble similarity (Fig. 5A), as described previously (Miller et al. 2014). Given that different visual information is assumed to be encoded by different neuronal ensembles, larger correlations between ensembles (during different visual stimuli) imply lower stimulus discrimination performance. Therefore, we compared frame–frame correlation at different states (i.e., LED-off or LED-on) to evaluate the role of PV neurons in the regulation of stimulus-discrimination through the control of the multineuronal activity.

Without LED illumination, the correlation coefficients between ensembles for different stimuli were roughly one-tenth of those between neural ensembles for the same stimuli, in both PV-ArchT animals and control animals ($P < 0.0001$ in both cases, as results of Wilcoxon rank sum tests; average correlation coefficient and s.e. for each sample was; same stimuli in PV-ArchT ($n = 3918$ pairs), 0.351 ± 0.005 ; different stimuli in PV-ArchT ($n = 21593$), 0.038 ± 0.001 ; same stimuli in control ($n = 3146$), 0.390 ± 0.007 ; different stimuli in control ($n = 17593$), 0.039 ± 0.0003). This supports our assumption that different types of visual information should be encoded by different population activity patterns, and supports the reliability of the values obtained by those analyses.

Next, we investigated the role of PV cells in the regulation of response reliability of multineuronal activity. Interestingly, when PV cells were optogenetically inactivated, the frame–frame

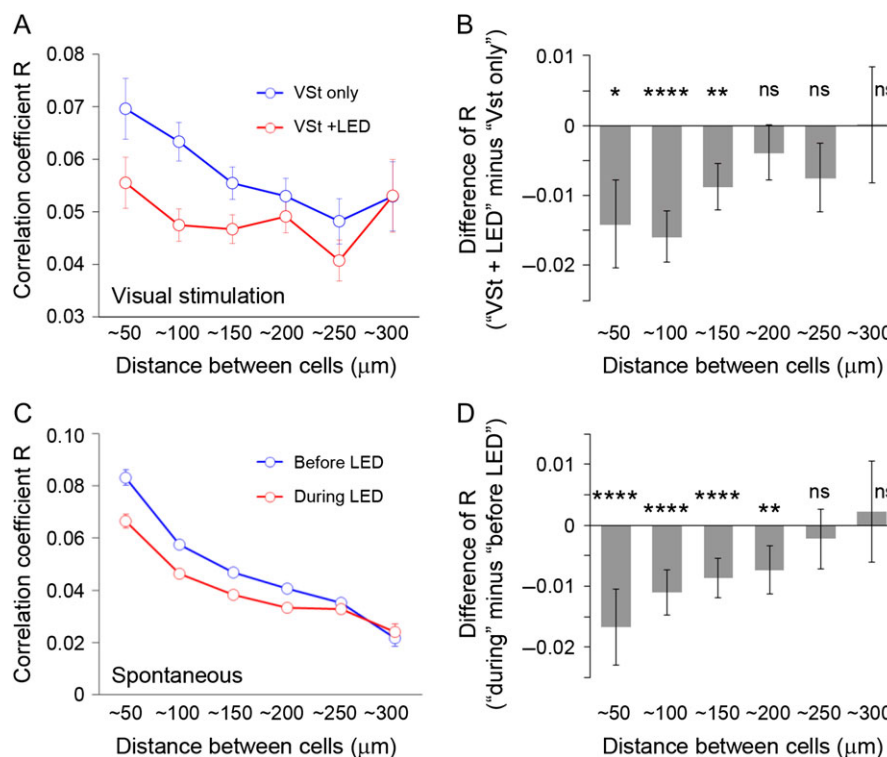


Figure 4. Locally existing temporal correlation is diminished by PV-cell suppression, with or without visual stimulation. Spatial modulation (i.e., the effect of cell-to-cell distance) of PV-dependent regulation of total correlations (R) was investigated during visual stimulation (A, B) and during spontaneous activity (C, D). (A, C) Correlation coefficients without or with LED (blue and red line, respectively) of PV-ArchT animals were plotted as a function of distance between cell bodies of GCaMP5-expressing neurons (number of pairs for each category (from ~50 to ~300 in this order): for (A), 436, 1027, 1238, 1039, 613, 261; for (C), 1650, 3998, 4842, 3982, 2580, 1059). Without LED illumination, the correlation coefficients decreased with cell–cell distance; correlation coefficients were high when cells were close together, and low when cells were distant. Although the similar tendency was seen during LED stimulation (suppression of PV neurons), cells at shorter distances showed more LED-driven decreases, whereas cells at greater distances did not show clear changes. (B, D) The degree of decrease in correlation coefficients by PV-cell suppression, plotted together with statistical results (one sample t-test to consider the difference from zero). The effects were dependent on cell–cell distances during visual stimulation (B) and spontaneous activity (D). VSt, visual stimulation; error bar, s.e.; ns, not significant; * $P < 0.05$; ** $p < 0.01$; **** $p < 0.0001$.

correlation during different stimuli increased significantly (Fig. 5B, C), indicating that the differential population activity patterns in response to different visual stimuli was diminished by PV-cell suppression (i.e., dissimilar patterns became more similar and correlated). The effect of the PV-cell suppression was consistently verified at the circuit level analysis (see Supplementary Fig. S7). These results indicate that PV interneurons regulate the response reliability of multineuronal ensembles, which may contribute to functions such as visual discrimination. While a role of PV cells in the regulation of visual recognition has been previously suggested (Lee et al. 2012), our results indicate one potential mechanism of how PV neurons could be involved in it, by regulating neuronal ensembles.

Spatial and Temporal Coregulation of Network Dynamics by PV Neurons

Although there has been a long-standing discussion of how neuronal synchrony, or temporal correlation, affects information coding by a population of neurons (Averbeck et al. 2006), there is still a paucity of data examining this question. Our results above support the hypothesis that the spatial gradient of network synchrony enhanced by the PV neurons might effectively sculpt spatial activity patterns, which may be important for information processing. To evaluate the actual impact of network synchrony on the response reliability of multineuronal activity, we investigated the relationship between total correlation (shared temporal dynamics between cells) and frame to frame correlation (spatially regulated neuronal ensemble)

(Fig. 6). To consider the relationship between temporal features and a spatial feature, we calculated the mean response of each circuit and analyzed tendencies of the observed circuits overall ($N = 8$ for PV-ArchT animals). For example, results of the change in frame to frame correlation for different angles of visual stimuli are summarized in Figure 6A, showing circuit-to-circuit variability of the effect of PV-cell suppression.

While the variability of ArchT expression level in each circuit might cause circuit-to-circuit difference in impact of LED illumination to the degree of the PV-cell suppression, the effects of PV-cell suppression to network synchrony and ensemble similarity could still be mechanistically linked.

To investigate this, we first compared the frame to frame correlation change during PV-cell suppression with the total correlation change. We found that these two variables were strongly and significantly correlated (Fig. 6B). At the same time, when considering frame–frame correlation during LED-off and -on trials separately, or even when the combined dataset was analyzed together, we found no significant correlation between frame–frame and total correlation (Fig. 6C), suggesting that those two factors are not necessarily always correlated. Moreover, we also found no significant correlation between changes in activity and those in frame to frame correlation (Fig. 6D), indicating that the tight link we observed between frame to frame correlation change and total correlation change is not an artifact and is not simply a result of the variability of the ArchT expression level. Together, these data indicate that the regulation of network synchrony by PV interneurons may directly contribute to maintaining response reliability of multineuronal activity.

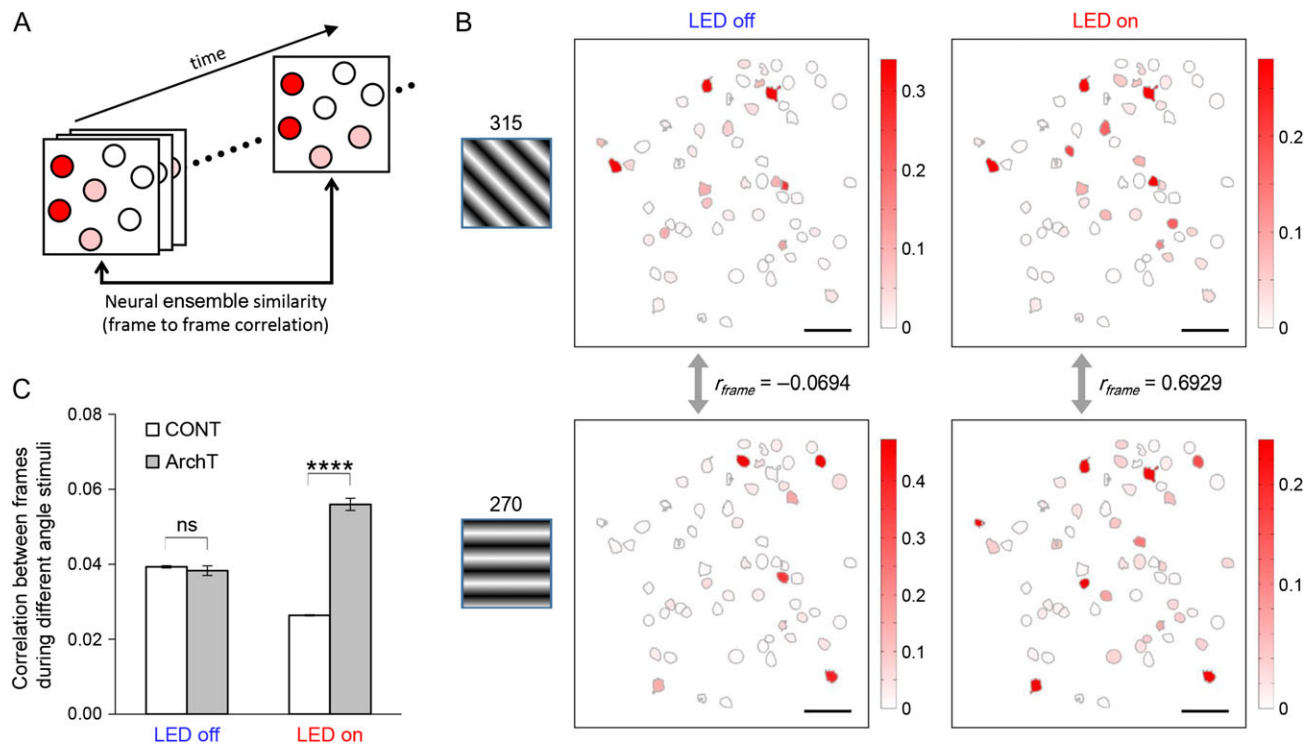


Figure 5. Neuronal ensembles evoked by visual stimuli are disturbed by PV-cell suppression. (A) Schematic illustrating how we compared similarity between neural ensembles. Population activity patterns at different time points (frames) were compared to calculate frame–frame correlation coefficient (r_{frame}). (B) Examples of neuronal ensembles disturbed by PV-cell suppression. Normally, as seen in the two left-hand panels, activity patterns during different visual stimuli (315°, top; 270°, bottom) were not similar and the frame–frame correlation was almost zero. On the other hand, as seen in the right-hand panels, more similar ensembles (and high correlation) were observed during PV-cell suppression (PV-ArchT animal). (C) PV-cell suppression significantly increased correlation coefficients between neuronal ensembles at different time points (i.e., different frames) while different angles of visual stimuli were presented. CONT, control animals ($N = 5$ animals; LED-off, $n = 17\,593$ pairs of neurons; LED-on, $n = 25\,348$); ArchT, PV-ArchT animals ($N = 8$; LED-off, $n = 21\,593$; LED-on, $n = 18\,429$); error bar, s.e.; ns, not significant; **** $P < 0.0001$.

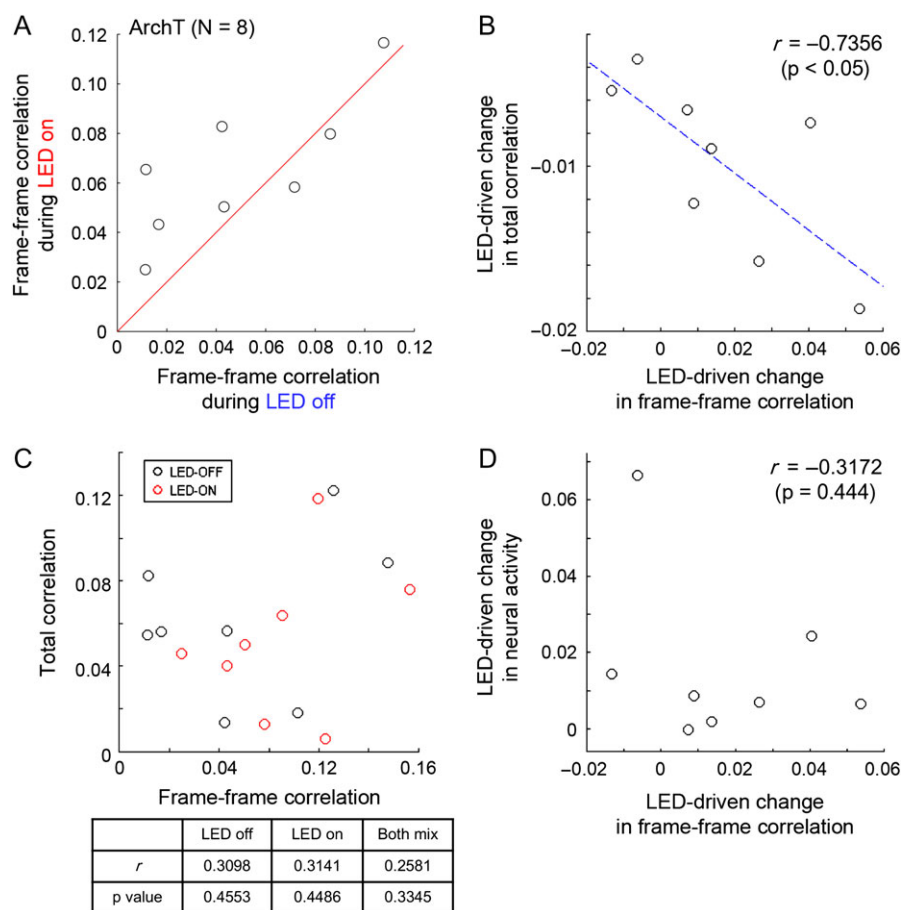


Figure 6. Spatial and temporal network dynamics are coregulated by PV neurons. To compare spatial dynamics (neural ensemble similarity) with other temporal dynamics statistically, we compared average values for each circuit ($N = 8$) in the PV-ArchT animals. Each circle corresponds to the average value for each circuit. (A) Summary of the effect of PV-cell suppression on frame-frame correlation between LED-on and LED-off. Red line indicates 1:1 ratio. (B) Frame-frame correlation change driven by PV-cell suppression was compared with change in total correlation. Blue dotted lines correspond to the results of line fitting (linear regression). r and P values are results of Pearson's correlation coefficient. (C) Raw values of frame-frame correlation were not directly correlated with raw values of total correlation, irrespective of LED-on/off or even when both were mixed for the analyses. To compare those values statistically, average values for each circuit ($N = 8$) of the PV-ArchT animals were compared. Each circle corresponds to the result of each circuit. (top) scatter plots representing the relationships. (bottom) summary of results of Pearson's correlation coefficient for LED-on/off, or both data mixed. (D) Frame-frame correlation change driven by PV-cell suppression was compared with change in neural activity. r and P values are results of Pearson's correlation coefficient.

Discussion

In the present study, we tested the hypothesis that dense inhibitory connections from PV interneurons to pyramidal cells might regulate spatio-temporal population activity patterns. To this end, we used *in vivo* two-photon imaging in mouse V1 to record activity from large neuronal populations during simultaneous optogenetic inactivation of the surrounding PV cells.

Our main result is that coactive neuronal ensembles are affected by PV-interneurons suppression. In particular, ensembles become less distinct from each other (more correlated) if inhibition is compromised (Fig. 5). This effect of inhibition at separating patterns of activity is reminiscent of lateral inhibition, a well-demonstrated function of inhibitory circuits whereby similar sensory stimuli generate more distinct patterns of activity. Thus, at the network level, inhibitory circuits could implement pattern separation (Kohonen 1982). This orthogonalization could be used to perform self-organizing mapping, or, more generally, to enable neural circuit dynamics to better occupy a larger multidimensional space. In addition to this main finding, our data (Fig. 2G–J; see Supplementary Fig. S2E–G) confirm the importance of PV neurons in the regulation of network coactivity,

which is consistent with previous observations that PV neurons regulate network correlations (Cardin et al. 2009; Sohal et al. 2009). Moreover, we found that network coactivity regulated by PV interneurons is distance-dependent (Fig. 4). We also found that the response reliability of multineuronal activity was regulated by PV neurons, a function that may underlie the role of PV neurons in visual discrimination, as suggested previously (Lee et al. 2012). These results altogether support the hypothesis that the spatial gradient of network synchrony enhanced by the PV neurons might effectively sculpt spatial activity patterns, an effect which may be important for information processing. Indeed, we observe that regulation of network coactivity (Figs 2–4) and the reliability of neuronal ensembles (Fig. 5) by PV interneurons are strongly and significantly correlated (Fig. 6). While network coactivity has been thought to be potentially important for computations in cortical circuits, these results indeed show that the spatio-temporal regulation by inhibitory interneurons may be an important mechanism for information processing.

Although outside the scope of this study, it will be interesting to further investigate the mechanism by which PV interneurons actually regulate network coactivity, lateral inhibition and

neuronal ensembles. To understand this further, one needs to functionally dissect the cortical circuit responses at higher temporal and spatial resolution, since it consists of complex wiring, recurrent circuits and disinhibitory connections by a multitude of different cell types. To carry out this, it also seems important to use optogenetic suppression methods with single cell resolution, while simultaneously imaging excitatory and inhibitory neurons.

Our results are at odds with our own previous study *in vitro*, where pharmacological blockage of inhibition in developing cortex resulted in increased network correlations in somatosensory cortex (Sippy and Yuste 2013). It is not straightforward to compare these results because, in addition to age, brain-region and methodological differences, the existence of complex inhibitory–inhibitory connections between different subtypes of inhibitory interneurons (Pfeffer et al. 2013) could complicate the effects. For instance, it is possible that other subtypes of cortical inhibitory neurons connecting to the PV cells, or interactions of multiple subtypes together, could generate opposing and/or stronger roles in the regulation of cortical synchrony.

One technical limitation with our results is that light illumination can cause nonhomogeneous optogenetic manipulation, which generally needs to be considered in all experiments using bulk illumination for optogenetics. Since the inhomogeneity of illumination in deeper brain area is milder than that near the surface (Chow et al. 2010), we used LED light at a tilted angle (see Methods) (Atallah et al. 2012) so that light traveled through a certain distance before it reached the target area. To further investigate the mechanism more quantitatively or to understand spatial regulation more precisely, future work should use recently developed methods that are based on two-photon excitation with single-cell resolution (Wilson et al. 2012; Packer et al. 2013, 2015).

Neuronal computations are also modulated by a balance between external stimuli (e.g., sensory stimuli) and internal (or spontaneous) patterns. This inspired us to examine the effect of PV neurons on both spontaneous and visually evoked activity. Our results suggest that PV neurons may consistently regulate correlated network activity during both spontaneous and visually evoked states, with suppression of PV neuron activity leading to a decrease in cell-to-cell correlations. This decrease could occur by the appearance of spurious correlation due to unsuppressed noisy spikes in the network, perhaps due to the stochastic nature of synaptic transmission. Regardless of the exact synaptic or circuit mechanisms, these results support the hypothesis that synchrony control by PV neurons might depend on the anatomical and/or functional connectivity within the local cortical network. Interestingly, while neural activity during visual stimulation was increased by PV-cell suppression, there was no significant increase of spontaneous activity during PV-cell suppression, suggesting that the regulation of the temporal correlation by PV neurons can be independent of firing rate of the neural network. Moreover, our analyses support this hypothesis since the effect of PV-cell suppression was local (Fig. 4). Because PV neurons possess a dense inhibitory connection to nearby postsynaptic excitatory neurons (Packer and Yuste 2011; Karnani et al. 2014), common inputs to cell pairs from the PV neurons are likely to be responsible for regulating the network correlation.

Although we performed these experiments with anesthetized animals, the effect of inhibitory circuits on neuronal ensembles is also likely occurring during awake states (irrespective of the cognitive or behavioral state), because the mechanism we uncover is probably based on an anatomical network structure that probably underlies neural computation in awake animals too. It would be interesting to test which

additional mechanisms or neural circuits enable unique brain activity during certain awake states, a question that can be tackled (Fu et al. 2014; Roth et al. 2016). For example, visual attention affects network correlation in V1, which potentially results in enhanced neural computation (Herrero et al. 2013; Ruff and Cohen 2014). Thus, the role of PV neurons in regulating network correlation may also contribute to the attention-dependent improvement in cognitive performance.

Finally, inhibitory interneurons are also thought to be important in maintaining a normal brain state and preventing psychiatric disorders (Hashimoto et al. 2008; Hamm et al. 2011; Marín 2012). Alterations in PV neurons are present in postmortem brain samples from schizophrenia patients (Hashimoto et al. 2008), and decreased sensory-evoked gamma and low-frequency phase locking has been demonstrated in chronic schizophrenia patients (Hamm et al. 2011). The present report can provide a link between these findings. Taken together, it merits further investigation whether microcircuit-level network correlations are also impaired in persons with schizophrenia, as suggested by a recent study in rodent models of psychotic brain states (Hamm et al. 2017).

Supplementary Material

Supplementary data are available at *Cerebral Cortex* online.

Funding

Supported by the NEI (DP1EY024503, R01EY011787), NIMH (R01MH101218, R01MH100561), Japan Science and Technology Agency, PRESTO (to M.A.), and Ministry of Education, Culture, Sports, Science and Technology, Japan (grant number 15K18341 to M.A.). This material is also based upon work supported by, or in part by, the US Army Research Laboratory and the US Army Research Office under Contract (W911NF-12-1-0594).

Notes

We thank T. Komiyama, E. Mukamel, M. Matsuzaki, and Y. Tanaka for providing the MATLAB codes. We thank H. Hirase, N. Takata, T. Tsumoto, K. Sohya, K. Kitamura, T. Hirabayashi, N. Nagai, Y. Arai, T. Wazawa, H. Hashimoto, A. Kasai, K. Seiriki, Y. Morishima, I. Sato, M. Morishima, and S. Kashiwagi for technical advice. We thank the Bionanophotonics Consortium under the MEXT Scientific Research on Innovative Area “Spying Minority in Biological Phenomena” (Grant Number, 23115001) for assistance in confocal microscopy. We also thank members of the laboratory for help, especially J. Miller, E. Fino, T. Sippy, A. Woodruff, and M. Karnani for technical advice, D. Peterka for discussion and optical setup, A. Packer, C. Stern-Ascher, I. Ayzenshtat, B. Shababo, and J. Jackson for MATLAB analyses, and Y. Shin for help with mice. *Conflict of Interest*: None declared.

References

- Abeles M. 1991. *Corticonics: neural circuits of the cerebral cortex*. Cambridge: Cambridge University Press.
- Akerboom J, Chen T-W, Wardill TJ, Tian L, Marvin JS, Mutlu S, Calderón NC, Esposti F, Borguis BG, Sun XR, et al. 2012. Optimization of a GCaMP calcium indicator for neural activity imaging. *J Neurosci*. 32:13819–13840.
- Atallah BV, Bruns W, Carandini M, Scanziani M. 2012. Parvalbumin-expressing interneurons linearly transform cortical responses to visual stimuli. *Neuron*. 73:159–170.

- Atallah BV, Scanziani M, Carandini M. 2014. Atallah et al. reply. *Nature*. 508:E3.
- Averbeck BB, Latham PE, Pouget A. 2006. Neural correlations, population coding and computation. *Nat Rev Neurosci*. 7: 358–366.
- Barthó P, Hirase H, Monconduit L, Zugaro M, Harris KD, Buzsáki G. 2004. Characterization of neocortical principal cells and interneurons by network interactions and extracellular features. *J Neurophysiol*. 92:600–608.
- Brainard DH. 1996. The psychophysics toolbox. *Spat Vis*. 10: 433–436.
- Cardin JA, Carlén M, Meletis K, Knoblich U, Zhang F, Deisseroth K, Tsai L, Moore CI. 2009. Driving fast-spiking cells induces gamma rhythm and controls sensory responses. *Nature*. 459: 663–667.
- Chelaru MI, Dragoi V. 2008. Efficient coding in heterogeneous neuronal populations. *Proc Natl Acad Sci U S A*. 105: 16344–16349.
- Chow BY, Han X, Dobry AS, Qian X, Chuong AS, Li M, Henninger MA, Belfort GM, Lin Y, Monahan PE, et al. 2010. High-performance genetically targetable optical neural silencing by light-driven proton pumps. *Nature*. 463:98–102.
- Cohen MR, Kohn A. 2011. Measuring and interpreting neuronal correlations. *Nat Neurosci*. 14:811–819.
- Connors BW. 1984. Initiation of synchronized neuronal bursting in neocortex. *Nature*. 310:685–687.
- Cossart R, Aronov D, Yuste R. 2003. Attractor dynamics of network UP states in the neocortex. *Nature*. 423:283–288.
- Delorme A, Makeig S. 2004. EEGLAB: an open source toolbox for analysis of single-trial EEG dynamics including independent component analysis. *J Neurosci Methods*. 134:9–21.
- Dombeck DA, Khabbaz AN, Collman F, Adelman TL, Tank DW. 2007. Imaging large-scale neural activity with cellular resolution in awake, mobile mice. *Neuron*. 56:43–57.
- El-Boustani S, Wilson NR, Runyan CA, Sur M. 2014. El-Boustani et al. reply. *Nature*. 508:E3–E4.
- Evangelidis GD, Psarakis EZ. 2008. Parametric image alignment using enhanced correlation coefficient maximization. *IEEE Trans Pattern Anal Mach Intell*. 30:1858–1865.
- Froudarakis E, Berens P, Ecker AS, Cotton RJ, Sinz FH, Yatsenko D, Saggau P, Bethge M, Tolias AS. 2014. Population code in mouse V1 facilitates readout of natural scenes through increased sparseness. *Nat Neurosci*. 17:851–857.
- Fu Y, Tucciarone JM, Espinosa JS, Sheng N, Darcy DP, Nicoll RA, Huang ZJ, Stryker MP. 2014. A cortical circuit for gain control by behavioral state. *Cell*. 156:1139–1152.
- Fujisawa S, Amarasingham A, Harrison MT, Buzsáki G. 2008. Behavior-dependent short-term assembly dynamics in the medial prefrontal cortex. *Nat Neurosci*. 11:823–833.
- Gonchar Y, Wang Q, Burkhalter A. 2007. Multiple distinct subtypes of GABAergic neurons in mouse visual cortex identified by triple immunostaining. *Front Neuroanat*. 1:3.
- Hamm JP, Dyckman KA, McDowell JE, Clementz BA. 2012. Precue fronto-occipital alpha phase and distributed cortical oscillations predict failures of cognitive control. *J Neurosci*. 32:7034–7041.
- Hamm JP, Gilmore CS, Picchetti NAM, Sponheim SR, Clementz BA. 2011. Abnormalities of neuronal oscillations and temporal integration to low- and high-frequency auditory stimulation in schizophrenia. *Biol Psychiatry*. 69:989–996.
- Hamm JP, Peterka DS, Gogos JA, Yuste R. 2017. Altered cortical ensembles in mouse models of schizophrenia. *Neuron*. 94: 153–167.e8.
- Han X, Chow BY, Zhou H, Klapoetke NC, Chuong A, Rajimehr R, Yang A, Baratta MV, Winkle J, Desimone R, et al. 2011. A high-light sensitivity optical neural silencer: development and application to optogenetic control of non-human primate cortex. *Front Syst Neurosci*. 5:18.
- Hashimoto T, Arion D, Unger T, Maldonado-Avilés JG, Morris HM, Volk DW, Mirmics K, Lewis DA. 2008. Alterations in GABA-related transcriptome in the dorsolateral prefrontal cortex of subjects with schizophrenia. *Mol Psychiatry*. 13:147–161.
- Herrero JL, Gieselmann MA, Sanayei M, Thiele A. 2013. Attention-induced variance and noise correlation reduction in Macaque V1 is mediated by NMDA receptors. *Neuron*. 78: 729–739.
- Hofer SB, Ko H, Pichler B, Vogelstein J, Ros H, Zeng H, Lein E, Lesica NA, Mrcic-Flogel TD. 2011a. Differential connectivity and response dynamics of excitatory and inhibitory neurons in visual cortex. *Nat Neurosci*. 14:1045–1052.
- Hofer SB, Ko H, Pichler B, Vogelstein J, Ros H, Zeng H, Lein E, Lesica NA, Mrcic-Flogel TD. 2011b. Differential connectivity and response dynamics of excitatory and inhibitory neurons in visual cortex. *Nat Neurosci*. 14:1045–1052.
- Kadir SN, Goodman DFM, Harris KD. 2014. High-dimensional cluster analysis with the masked EM algorithm. *Neural Comput*. 26:2379–2394.
- Kaifosh P, Lovett-Barron M, Turi GF, Reardon TR, Losonczy A. 2013. Septo-hippocampal GABAergic signaling across multiple modalities in awake mice. *Nat Neurosci*. 16:1182–1184.
- Karnani MM, Agetsuma M, Yuste R. 2014. A blanket of inhibition: functional inferences from dense inhibitory connectivity. *Curr Opin Neurobiol*. 26:96–102.
- Kerlin AM, Andermann ML, Berezovskii VK, Reid RC. 2010. Broadly tuned response properties of diverse inhibitory neuron subtypes in mouse visual cortex. *Neuron*. 67:858–871.
- Kitamura K, Judkewitz B, Kano M, Denk W, Häusser M. 2008. Targeted patch-clamp recordings and single-cell electroporation of unlabeled neurons in vivo. *Nat Methods*. 5:61–67.
- Ko H, Hofer SB, Pichler B, Buchanan KA, Sjöström PJ, Mrcic-Flogel TD. 2011. Functional specificity of local synaptic connections in neocortical networks. *Nature*. 473:87–91.
- Kohonen T. 1982. Self-organized formation of topologically correct feature maps. *Biol Cybern*. 43:59–69.
- Lee S-H, Kwan AC, Dan Y. 2014. Interneuron subtypes and orientation tuning. *Nature*. 508:E1–E2.
- Lee S-H, Kwan AC, Zhang S, Phoumthipphavong V, Flannery JG, Masmanidis SC, Taniguchi H, Huang ZJ, Zhang F, Boyden ES, et al. 2012. Activation of specific interneurons improves V1 feature selectivity and visual perception. *Nature*. 488: 379–383.
- Marín O. 2012. Interneuron dysfunction in psychiatric disorders. *Nat Rev Neurosci*. 13:107–120.
- Mattis J, Tye KM, Ferenczi EA, Ramakrishnan C, O’Shea DJ, Prakash R, Gunaydin LA, Hyun M, Fenno LE, Gradinaru V, et al. 2012. Principles for applying optogenetic tools derived from direct comparative analysis of microbial opsins. *Nat Methods*. 9:159–172.
- McCormick DA, Contreras D. 2001. On the cellular and network bases of epileptic seizures. *Annu Rev Physiol*. 63:815–846.
- Miller JK, Ayzenshtat I, Carrillo-Reid L, Yuste R. 2014. Visual stimuli recruit intrinsically generated cortical ensembles. *Proc Natl Acad Sci U S A*. 111:E4053–E4061.
- Mukamel E, Nimmerjahn A, Schnitzer M. 2009. Automated analysis of cellular signals from large-scale calcium imaging data. *Neuron*. 63:747–760.

- Niell CM, Stryker MP. 2010. Modulation of visual responses by behavioral state in mouse visual cortex. *Neuron*. 65:472–479.
- Ohki K, Chung S, Ch'ng YH, Kara P, Reid RC. 2005. Functional imaging with cellular resolution reveals precise micro-architecture in visual cortex. *Nature*. 433:597–603.
- Ohki K, Chung S, Kara P, Hübener M, Bonhoeffer T, Reid RC. 2006. Highly ordered arrangement of single neurons in orientation pinwheels. *Nature*. 442:925–928.
- Packer AM, Peterka DS, Hirtz JJ, Prakash R, Deisseroth K, Yuste R. 2012. Two-photon optogenetics of dendritic spines and neural circuits. *Nat Methods*. 9:1202–1205.
- Packer AM, Roska B, Häusser M. 2013. Targeting neurons and photons for optogenetics. *Nat Neurosci*. 16:805–815.
- Packer AM, Russell LE, Dalgleish HWP, Häusser M. 2015. Simultaneous all-optical manipulation and recording of neural circuit activity with cellular resolution in vivo. *Nat Methods*. 12:140–146.
- Packer AM, Yuste R. 2011. Dense, unspecific connectivity of neocortical parvalbumin-positive interneurons: a canonical microcircuit for inhibition? *J Neurosci*. 31:13260–13271.
- Peters AJ, Chen SX, Komiyama T. 2014. Emergence of reproducible spatiotemporal activity during motor learning. *Nature*. 510:263–267.
- Pfeffer CK, Xue M, He M, Huang ZJ, Scanziani M. 2013. Inhibition of inhibition in visual cortex: the logic of connections between molecularly distinct interneurons. *Nat Neurosci*. 16:1068–1076.
- Preuss T, Kaas J. 1996. Parvalbumin-like immunoreactivity of layer V pyramidal cells in the motor and somatosensory cortex of adult primates. *Brain Res*. 712:353–357.
- Prince DA. 1978. Neurophysiology of epilepsy. *Annu Rev Neurosci*. 1:395–415.
- Roth MM, Dahmen JC, Muir DR, Imhof F, Martini FJ, Hofer SB. 2016. Thalamic nuclei convey diverse contextual information to layer 1 of visual cortex. *Nat Neurosci*. 19:299–307.
- Rudy B, Fishell G, Lee S, Hjerling-Leffler J. 2011. Three groups of interneurons account for nearly 100% of neocortical GABAergic neurons. *Dev Neurobiol*. 71:45–61.
- Ruff DA, Cohen MR. 2014. Attention can either increase or decrease spike count correlations in visual cortex. *Nat Neurosci*. 17:1591–1597.
- Sanchez-Vives MV, McCormick DA. 2000. Cellular and network mechanisms of rhythmic recurrent activity in neocortex. *Nat Neurosci*. 3:1027–1034.
- Sippy T, Yuste R. 2013. Decorrelating action of inhibition in neocortical networks. *J Neurosci*. 33:9813–9830.
- Sohal VS, Zhang F, Yizhar O, Deisseroth K. 2009. Parvalbumin neurons and gamma rhythms enhance cortical circuit performance. *Nature*. 459:698–702.
- Sohya K, Kameyama K, Yanagawa Y, Obata K, Tsumoto T. 2007. GABAergic neurons are less selective to stimulus orientation than excitatory neurons in layer II/III of visual cortex, as revealed by in vivo functional Ca²⁺ imaging in transgenic mice. *J Neurosci*. 27:2145–2149.
- Vogelstein JT, Packer AM, Machado TA, Sippy T, Babadi B, Yuste R, Paninski L. 2010. Fast nonnegative deconvolution for spike train inference from population calcium imaging. *J Neurophysiol*. 104:3691–3704.
- Wilson NR, Runyan CA, Wang FL, Sur M. 2012. Division and subtraction by distinct cortical inhibitory networks in vivo. *Nature*. 488:343–348.
- Zhu Y, Qiao W, Liu K, Zhong H, Yao H. 2015. Control of response reliability by parvalbumin-expressing interneurons in visual cortex. *Nat Commun*. 6:6802.